

State-Selective Preparation of NO_2^+ and the Effects of NO_2^+ Vibrational Mode on Charge Transfer with NO^\dagger

Brady Uselman, Jianbo Liu, Jason Boyle, and Scott Anderson*

Department of Chemistry, University of Utah, 315 S. 1400 E. Rm 2020, Salt Lake City, Utah 84112

Received: June 17, 2005; In Final Form: July 25, 2005

Two color resonance-enhanced multiphoton ionization (REMPI) scheme of NO_2 through the $E^2\Sigma_u^+(3p\sigma)$ Rydberg state was used to prepare NO_2^+ in its ground and (100), (010), (02⁰0), (02²0), and (001) vibrational states. Photoelectron spectroscopy was used to verify >96% state selection purity, in good agreement with results of Bell et al.¹ for a similar REMPI scheme. The effects of NO_2^+ vibrational excitation on charge transfer with NO have been studied over the center-of-mass collision energy (E_{col}) range from 0.07 to 2.15 eV. Charge transfer is strongly suppressed by collision energy at $E_{\text{col}} < \sim 0.25$ eV but is independent of E_{col} at higher energies. Mode-specific vibrational effects are observed for both the integral and differential cross-sections. The NO_2^+ bending vibration strongly enhances charge transfer, with enhancement proportional to the bending quantum number, and is not dependent on the bending angular momentum. The enhancement results from increased charge transfer probability in large impact parameter collisions that lead to small deflection angles. The symmetric stretch also enhances reaction at low collision energies, albeit less efficiently than the bend. The asymmetric stretch has virtually no effect, despite being the highest-energy mode. A model is proposed to account for both the collision energy and the vibrational state dependence.

I. Introduction

As part of a continuing study of vibrational-mode effects on polyatomic reactions, we are studying energy transfer and reaction dynamics in several simple reactions of NO_2^+ . NO_2^+ is an important ion in electrophilic nitration, and this sort of NO_2^+ chemistry has been studied extensively in both gas and solution phases, with both experimental and theoretical approaches.^{2–11} On the other hand, not many NO_2^+ reactions have been studied from a dynamical perspective.¹² One that has is the exoergic charge transfer (CT) reaction of NO_2^+ with NO . Fehsenfeld and co-workers¹³ reported a flowing afterglow study at 300 K, where the rate constant was reported to be 2.9×10^{-10} cm³/mol–s for ground-state NO_2^+ . A later drift tube study by Durup-Ferguson et al.¹⁴ used different buffer gases and drift potentials to show that CT is enhanced by NO_2^+ vibrational excitation. There is a large geometry change accompanying neutralization of NO_2^+ (NO_2^+ , linear; NO_2 , bent at 134°), thus an effect of NO_2^+ bending excitation is not unexpected. In a similar vein, Clemmer and Armentrout showed by quenching experiments that the endoergic CT reaction of NO_2^+ with trifluorotoluene can be driven by NO_2^+ vibrational (presumably bending) excitation. The purpose of this paper is to explore the effects on CT of all three NO_2^+ vibrational modes and how the effects change as collision energy is varied over a large range.

Grant, Pratt, and co-workers have recently reported several spectroscopic studies indicating that NO_2 can be state-selectively ionized by resonance-enhanced multiphoton ionization (REMPI) through the $E^2\Sigma_u^+(3p\sigma)$ Rydberg state.^{1,15,16} Their work indicates that all three modes can be populated with high purity, and for this paper, we have used a simplified version of their REMPI scheme to prepare mode-selectively excited NO_2^+ for reaction studies under beam conditions. We first demonstrate

that our REMPI scheme gives good state selection, then report on the effects of collision energy and NO_2^+ vibrational mode on the CT reaction with NO . In the following, we will denote the states as $(n_1 n_2 n_3)$, where n_i are the number of quanta in the ν_1^+ (symmetric stretch), ν_2^+ (bend), and ν_3^+ (asymmetric stretch) modes, respectively. For the bend overtone state, (020), there are Σ and Δ components, indicated by the associated bending angular momentum: (02⁰0) and (02²0), respectively.

II. Experimental Section

The experiments were performed in an instrument that can be configured either as a time-of-flight (TOF) photoelectron/mass spectrometer or as a guided-ion-beam tandem mass spectrometer. Both the photoelectron spectrometry^{17,18} and ion-beam configurations^{19,20} have been described previously, along with operation, calibration, and data analysis procedures. In both configurations, $\text{NO}_2^+(v)$ was generated by two-color, three-photon ionization of a pulsed, skimmed molecular beam of NO_2 (Matheson Tri-Gas 99.5%) seeded in He at a 1:5 ratio. Two dye lasers (Continuum ND6000 and ND60) were pumped by a single Nd:YAG laser (Continuum NY-82S). The lower-energy photons ($\omega_1 = 23\,097$ cm⁻¹) were generated by mixing 730 nm from one dye laser with residual Nd:YAG fundamental in a KD*P crystal, giving 5–6 mJ/pulse. The higher-energy photons ($\omega_2 = 32\,527$ – $34\,885$ cm⁻¹) were generated by frequency-doubling the output of the second dye laser, giving 2–4 mJ/pulse. Below, we separately describe the methodologies for NO_2^+ state selection and for the ion–molecule studies.

A. REMPI and State Selection. Figure 1 shows the scheme for REMPI and a typical spectrum. The first photon (ω_1) excites NO_2 to an intermediate level lying in a near-continuum resulting from vibronic mixing of levels of the ground, 2A_2 , 2B_1 , and 2B_2 , states. To eliminate predissociation at this level, ω_1 is kept below the predissociation limit ($\sim 25\,100$ cm⁻¹).²¹ Next, a UV

[†] Part of the special issue “William Hase Festschrift”.

* To whom correspondence should be addressed.

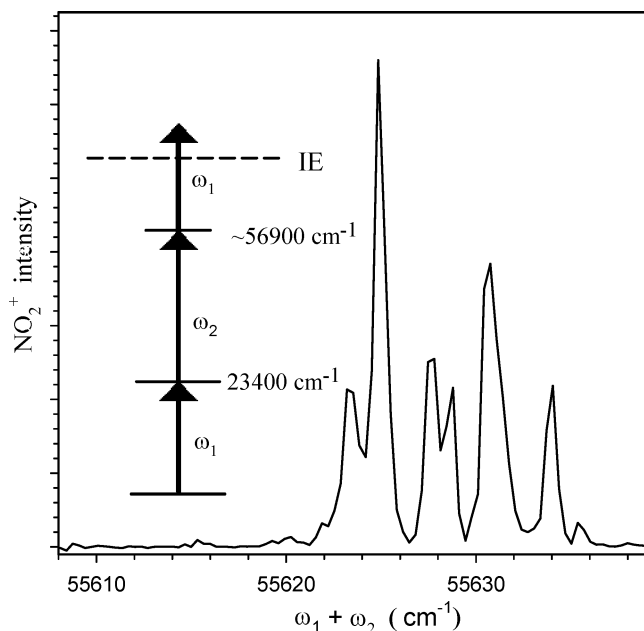


Figure 1. REMPI spectra taken for ground state of NO_2 . Inset: two-color pumping scheme.

photon (ω_2) is used to reach a specific vibrational level of the $E\ ^2\Sigma_u^+(3p\sigma)$ Rydberg state. Finally, ionization is achieved by absorption of an additional photon of ω_1 or ω_2 . The REMPI spectra were taken in the TOF spectrometry configuration, where ions are produced inside and near one end of a μ -metal magnetic shielding tube. For TOF mass spectrometry, grids are used to accelerate the ions toward a microchannel plate detector located ~ 0.75 m from the ionization region. REMPI spectra for production of NO_2^+ parent ions were acquired by integrating the corresponding TOF peak, while scanning the second laser (ω_2), keeping ω_1 fixed to maximize ion intensity. This type of scan probes levels of the $E\ ^2\Sigma_u^+(3p\sigma)$ intermediate state, with energies corresponding to $\omega_1 + \omega_2$. Rotational structure was partially resolved, and the most intense transition in each vibrational band was chosen for both photoelectron spectroscopy measurement and generation of ions for reaction studies.

B. Time-of-Flight Photoelectron Spectroscopy. The setup for the photoelectron spectroscopy was identical to that for TOF mass spectrometry. For the relatively intense transitions through the (000), (0n0), and (001) levels of the $E\ ^2\Sigma_u^+(3p\sigma)$ Rydberg intermediate state, no acceleration potentials were used to aid electron collection, and collection efficiency is $\sim 10^{-4}$, determined by the solid angle subtended by the detector. For the weaker transition through the (100) level, a repeller voltage was used to improve collection efficiency, and the effect on the TOF was calibrated by varying the voltage from 0.25 to 2.0 V. The photoelectron signal was preamplified, then averaged over 5000 laser shots by a Tektronix 500M digital oscilloscope, running at a 2.5 G sample/s acquisition rate, and finally transferred to a computer for analysis. To correct for the signal from scattered laser light and for baseline curvature in the oscilloscope, we also measured background spectra with the molecular beam off.

Analysis of the photoelectron spectra is simple in this case, because the ionization out of the $3p\sigma$ Rydberg state is quite diagonal, i.e., there is a strong propensity to preserve the $3p\sigma$ vibrational state in the ion. Because ionization of the $3p\sigma$ intermediate can occur by absorption of an additional photon of either ω_1 or ω_2 , each spectrum is dominated by two peaks with quite distinct TOFs, reflecting the > 1 eV energy difference between ω_1 and ω_2 . The TOF spectra were converted to energy

spectra using the expression

$$\text{KE} = \frac{m_e \left(\frac{L}{t - t_0} \right)^2}{2} \quad (1)$$

where KE is the kinetic energy of photoelectron, L is the length of the flight path, t is the measured flight time, t_0 is an adjustable parameter representing the actual time of the ionization event, and m_e is the mass of the electron. The L and t_0 parameters were obtained by fitting the two peaks in the spectrum for the $3p\sigma$ (000) intermediate. On the basis of the results of Bell et al.,¹ these peaks are assumed to result from production of ground-state NO_2^+ by ionization of the $3p\sigma$ (000) level by a final photon of ω_1 or ω_2 . The resulting L value is close to the physical length of the flight path, and t_0 is nearly 2 orders of magnitude smaller than t . The calibrated parameters were then used to analyze the results for the other $3p\sigma$ vibrational levels. The absolute accuracy of the TOF to KE conversion is estimated to be ± 18 meV.

For this study, we did not make much effort to achieve high photoelectron energy accuracy or resolution, because higher-resolution results have been reported for ionization out of the same $E\ ^2\Sigma_u^+(3p\sigma)$ intermediate state.¹ This previous study used a magnetic bottle photoelectron spectrometer and therefore also had much higher sensitivity for minor peaks in the photoelectron spectra (PES). The motivation for our PES study was simply to verify that good state selection is achieved using our slightly different REMPI scheme. In their study, ω_1 was kept low enough in energy that it could not ionize the $3p\sigma$ levels, allowing only the $\omega_1 + \omega_2 + \omega_2$ ionization route. We used $\omega_1 \approx 1000$ cm^{-1} higher in energy (and ω_2 correspondingly lower), opening the $\omega_1 + \omega_2 + \omega_1$ ionization channel and thereby increasing the ion intensity, which is important in the ion–molecule reaction studies. In principle, the ion state distribution should depend only on the Franck–Condon factors for ionization of the $3p\sigma$ levels and not on the route used to populate them. Nonetheless, we felt it prudent to verify NO_2^+ state selection, and low resolution spectra suffice for this purpose.

C. Ion–Molecule Reaction Studies. NO_2^+ cations were generated by REMPI inside a radio frequency (rf) quadrupole ion guide. At the exit of this guide, the beam is energy- and mass-filtered by TOF gating using a split pair of ion lenses, resulting in a narrow kinetic energy spread of ~ 0.15 eV. Next, the ions enter a two-segment, eight-pole rf ion guide. The first guide segment passes through a scattering cell, 10 cm in length, filled to a pressure of 5×10^{-5} Torr with the NO reactant (Matheson Tri-Gas 99%). Product ions and unreacted primary ions are collected by this ion guide, then pass into the second, longer segment where TOF is used to measure the velocity distributions of reactant and product ions. Finally, ions are collected, mass-filtered, and detected. Because we are measuring subtle effects, it is important to minimize systematic variations in experimental conditions that might be caused by drifting potentials, changes in laser intensity or focal position, and so forth. For each state, we cycled through the series of collision energy (E_{col}) values several times. For a check on reproducibility, we measured the cross-sections for the ground state at the beginning of each complete experimental run and measured the entire set of cross-sections versus E_{col} and vibrational state several times on separate days.

For integral cross-section measurements, the ion guides were operated at high rf amplitude with a 1 V potential drop between the scattering cell and TOF segments of the guide, to aid in collection of slow ions. Integral cross-sections were calculated

from the ratio of reactant and product ion intensities, the target gas pressure, and the effective length of the target gas cloud. The effective length factor was determined by calibration, using the well-established cross-section for the $\text{Ar}^+ + \text{D}_2 \rightarrow \text{ArD}^+ + \text{D}$ reaction,²² and is within 10% of the geometric length of the scattering cell (Chui, 1995 #198). The integral cross-sections are estimated to have absolute uncertainties of $\sim 20\%$, mostly from possible collection efficiency issues (see below). The relative uncertainties for comparing cross-sections are somewhat better and are indicated below.

The TOF data can be converted to product ion axial velocity distributions, i.e., the projection of the product ion velocity distribution on the ion guide axis. In our experimental geometry, the relative velocity of the reactants and the velocity of the center-of-mass in the lab (V_{CM}) are both coaxial with the ion guide, on average. As a consequence, considerable dynamical information can be gleaned directly from the axial velocity (v_{axial}) distributions. For example, if reaction is mediated by a complex with a lifetime ($\tau_{\text{collision}}$) that is long in comparison to its rotational period (τ_{rotation}), the resulting v_{axial} distribution must be symmetric about V_{CM} . Conversely, an asymmetric v_{axial} distribution is a clear sign that the reaction is not mediated by a long-lived complex and also reveals the predominant scattering mechanisms (i.e., forward- or back-scattering). Finally, the deviation of the velocity distribution from V_{CM} is a measure of the maximum energy going into recoil in the forward and backward scattering directions.

III. Results

A. REMPI and PES Data. Figure 1 shows an example of our REMPI spectra, in this case, for ionization via the vibrationless level of the $E^2\Sigma_u^+(3p\sigma)$ state. As shown, we partially resolve the (J, K) rotational structure of the transition; however, rotational assignment is nontrivial, because the identity of the first intermediate level populated by ω_1 is unknown. For our purpose, the most important requirement is large intensities of vibrationally state-selected NO_2^+ ; therefore in the PES and ion-molecule reaction studies, we simply pumped the most intense rotational transition in each $3p\sigma$ vibrational band. Rotational intensities largely reflect the rotational population in the seeded supersonic NO_2 beam; thus, the resulting NO_2^+ rotational distribution should be similar for all NO_2^+ vibrational states, with a significant population only for $E_{\text{rot}} < \sim 10$ meV. Because E_{rot} is roughly constant and small compared to our collision and vibrational energies, no rotational effects are expected,^{23–28} and we made no attempt to either assign or vary the ion rotational levels produced.

Figure 2 shows the photoelectron spectra collected when ionizing NO_2 through the indicated vibrational levels of the $3p\sigma$ intermediate. The ionization is essentially diagonal, i.e., there is a single photoelectron peak, and the peak energies are consistent with NO_2^+ being generated in the same vibrational state that was populated in the $3p\sigma$ Rydberg intermediate. The magnetic bottle photoelectron spectra of Bell et al.¹ are similar, but because they have higher sensitivity, they were able to observe low-intensity nondiagonal ionization transitions, and their measured NO_2^+ vibrational distributions are given in Table 1. The important point is that for all states, the state selection purity is $\geq 96\%$. This purity level is high enough that we have not attempted to correct the ion-molecule cross-sections for the small nondiagonal populations. Neither we nor Bell et al. measured PES for pumping through the (02^00) and (02^20) bending overtone levels; however, since there is nothing in the REMPI spectra suggesting that the bend overtones are anomalous,

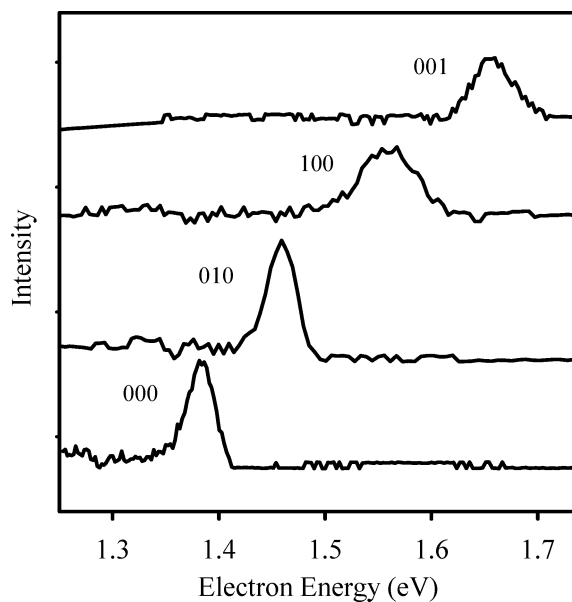


Figure 2. Photoelectron spectra showing production of NO_2^+ in its ground state and in the fundamental levels of the three vibrational modes.

TABLE 1: Pumping Wavelengths and Resulting NO_2^+ State Purity

ω_1 (cm^{-1})	ω_2 (cm^{-1})	$3p\sigma$ vibrational level	NO_2^+ vibrational distribution ^a	mode description	vibrational energy (meV)
23097	32527	000	(000) 97%; (020) 3%	ground state	0
23093	33158	010	(010) 99%; (000) 1%	bend	78
23097	33759	02^20	(02^20) 100%	bend	153
23097	33771	02^00	(02^00) 100%	bend	155
23097	33927	100	(100) 96%; (000) 1%; (200) 1%; (300) 1%	symmetric stretch	170
23097	34885	001	(001) 99%; (000) 1%	asymmetric stretch	290

^a Vibrational-state purity from high-resolution photoelectron spectroscopy results of Bell et al.¹

ous, we assume that ionization is also largely diagonal for those levels. The reactivity results below support this assumption.

B. Reaction of $\text{NO}_2^+(v)$ with NO. 1. *Reaction Coordinate: Ab Initio and $N^{18}\text{O}$ Reaction Results.* Charge transfer is the only energetically accessible product channel for $\text{NO}_2^+ + \text{NO}$ in the collision energy range from 0.07 to 2.15 eV



To aid interpretation of the experiments, we looked for possible $[\text{NO}_2\text{-NO}]^+$ complexes that might mediate reaction, and the results are shown in Figure 3, with energetics taken from QCISD(T)/6-311+G** calculations at geometries optimized at the MP2/6-31G* level of theory, and zero-point energies (ZPE) from MP2/6-31G* frequency calculations. The only complex found by straightforward optimization from several different starting geometries is an ONO-NO^+ structure bound by 0.74 eV relative to reactants. The ONO bend angle (136.1°) in this complex is similar to that in free neutral NO_2 (134°), and as this angle suggests, only $\sim 5\%$ of the Mulliken charge is on the NO_2 moiety. This structure is, therefore, a weakly bound complex of the charge transfer products. The structure of this

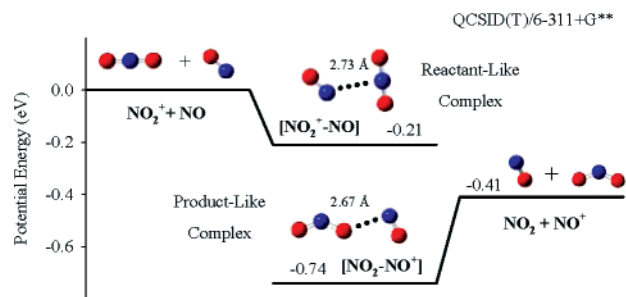


Figure 3. Schematic reaction coordinate for $\text{NO}_2^+ + \text{NO}$. Energies are derived from QCISD(T)/6-311+G** calculations, including MP2/6-31G* zero-point energies.

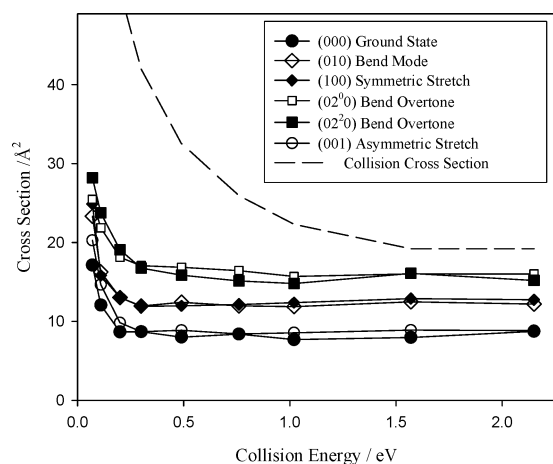


Figure 4. Charge transfer cross-sections vs E_{col} . Also shown is the estimated collision cross-section.

productlike complex raised the possibility that NO^+ production might occur by O transfer, in addition to CT. We were unable to find any low-lying transition state for O transfer; nonetheless, we looked experimentally for O transfer in the reaction of NO_2^+ with N^{18}O . Only N^{18}O^+ products are observed, i.e., CT is the only mechanism producing NO^+ in this energy range.

The CT exoergicity calculated at the QCISD(T) level is ~ 0.09 eV greater than the experimental value. The reactants, products, and productlike complex were also studied at the G3 level of theory, and in that case, the calculated exoergicity is ~ 0.06 eV too small, and the productlike complex is ~ 0.06 eV less strongly bound with respect to reactants than in the QCISD(T) result (i.e., nearly identical binding energy with respect to products).

For reasons discussed below, there is some reason to think that a reactantlike complex of the form $\text{NO}_2^+ \cdots \text{NO}$ might also play a role in the reaction. The methodology used to locate the reactantlike complex shown in Figure 3 is discussed below.

2. Integral Cross-Sections. The cross-sections for CT of NO_2^+ with NO are plotted in Figure 4 as a function of collision energy and the NO_2^+ vibrational state. Also shown for reference is the collision cross-section, $\sigma_{\text{collision}}$, estimated as the greater of the capture cross-section (σ_{capture}) and the hard-sphere cross-section ($\sigma_{\text{HardSphere}}$). $\sigma_{\text{HardSphere}}$ was calculated from the orientation-averaged contact radius of NO_2^+ and NO, assuming covalent radii for each atom, and exceeds σ_{capture} for $E_{\text{col}} > \sim 1.5$ eV.

For all reactant states, the cross-section is essentially E_{col} -independent for $E_{\text{col}} > 0.3$ eV but increases sharply at lower E_{col} . Excitation of the asymmetric stretch ((001) = 290 meV) has negligible effect on the cross-section except at the lowest E_{col} , where it enhances CT by $\sim 10\%$. Excitation of both the symmetric stretch ((100) = 170 meV) and the fundamental of the bend ((010) = 78 meV) enhance the cross-section by $\sim 50\%$

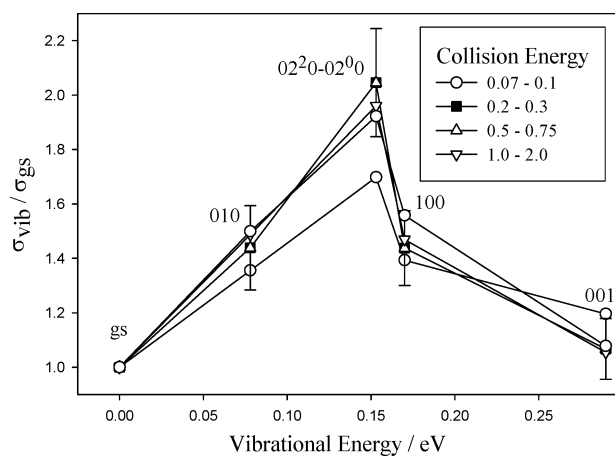


Figure 5. Vibrational enhancement factors vs $\text{NO}_2^+ E_{\text{vib}}$, for different ranges of collision energy.

over the entire E_{col} range. Finally, excitation of the bend overtone enhances CT by about a factor of 2, except at the lowest collision energies, where the relative enhancement is only $\sim 55\%$. The Σ symmetry ((02⁰) = 155 meV) and Δ symmetry ((02²) = 153 meV) overtones have effects that are identical within the uncertainty of the experiments.

To show how the vibrational effects vary with E_{col} , Figure 5 gives vibrational enhancement factors, i.e., ratios of cross-sections for NO_2^+ in particular vibrational states, to the ground-state cross-section. Because the (02⁰) and (02²) bend overtones have nearly identical energies and vibrational effects, we show just the average vibrational effect for the two states. The error bars were determined from reproducibility over several data sets. The only change in vibrational effects over our E_{col} range is a $\sim 20\%$ reduction in the effects at low E_{col} , even though this is where vibration makes up the largest fraction of the total reactant energy. As noted above, we do not have photoelectron spectroscopic measurements confirming the state selection purity for the bend overtones. The observation that the CT enhancement is linear in the bending quantum number supports the idea that these states are also produced with reasonable purity.

3. Recoil Velocity Distributions. Time-of-flight (TOF) data were collected for the NO^+ product ions for each reactant vibrational state and collision energy and converted to velocity distributions. LAB frame velocity distributions for reaction of ground-state NO_2^+ are plotted in Figure 6. The effects of NO_2^+ vibrational excitation on the velocity distribution will be discussed below. The solid vertical line in each frame of the figure gives the average velocity of the CM frame with respect to the lab, $\langle V_{\text{CM}} \rangle$. Because of the high symmetry of the experimental configuration, the LAB v_{axial} distributions can be approximately converted to the CM frame by simply subtracting $\langle V_{\text{CM}} \rangle$. In the discussion below, “forward” and “backward” are defined as product ions with axial velocities faster or slower, respectively, than $\langle V_{\text{CM}} \rangle$.

For $E_{\text{col}} \geq 0.48$ eV (i.e., in the range where σ_{CT} is E_{col} -independent), the v_{axial} distributions are asymmetric, peaking in the backward direction but extending well into the forward direction. The asymmetry implies that CT is direct, i.e., the collision time is less than τ_{rotation} for any complex that might form. Given the weak binding of the only complex we were able to locate, it is not surprising that the reaction would be direct at high E_{col} .

For $E_{\text{col}} \leq 0.26$ eV (in the range where σ_{CT} becomes E_{col} -dependent), the NO^+ distributions are symmetric about V_{cm} within the experimental uncertainty. Forward–backward sym-

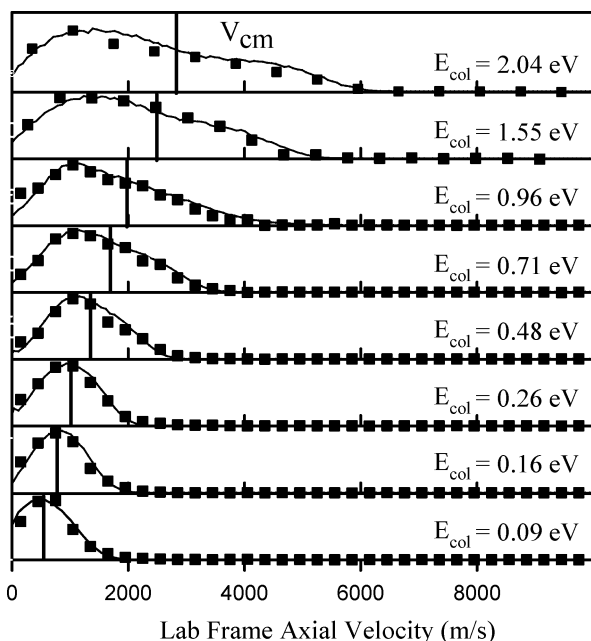


Figure 6. Axial recoil velocity distributions for NO^+ at different E_{col} . Solid symbols: experimental. Solid line: simulation based on the osculating complex model. Heavy vertical line: $\langle V_{\text{CM}} \rangle$.

metry is a necessary but not a sufficient condition to infer a complex-mediated mechanism, suggesting that the increasing cross-section at low E_{col} might signal transition to such a mechanism. Alternatively, the apparent forward–backward symmetry might simply be coincidental or might result if the recoil energy (E_{recoil}) is low enough that the asymmetry is masked by the experimental E_{col} distribution.

To address the issue of experimental broadening and to extract more insight from the v_{axial} distributions, it is necessary to fit the data. The fitting program is simply a Monte Carlo-based simulation of the experiment, including the ion and target gas velocity distributions, target rotational energy distribution, appropriate Jacobian factors, and so forth.¹⁹ A model recoil energy and angular distribution is put through the simulation and adjusted until the resulting v_{axial} distribution fits the experimental data. For the data here, we used a model designed for the case where the mechanism changes from complex-mediated to direct with increasing E_{col} . In the model, the angular distribution is described by the osculating complex model,³⁰ which assumes formation of a short-lived collision complex, with rotational angular momentum equal to the orbital angular momentum of the collision (the reactant rotational angular momentum is negligible). This rotating collision complex is assumed to decay to products with a lifetime, $\tau_{\text{collision}}$, and recoil energy distribution, $P(E_{\text{recoil}})$. Here, $P(E_{\text{recoil}})$ is assumed to be a Gaussian distribution controlled by width and peak value parameters defined in terms of the total available energy in the CT channel (E_{avail}). In this model, the degree of forward–backward symmetry depends on the ratio $\tau_{\text{collision}}/\tau_{\text{rotation}}$, where τ_{rotation} is calculated from the largest moment of inertia for the productlike collision complex (Figure 3) and the angular momentum, in turn estimated from the magnitude of the capture cross-section and E_{col} . The fitting results are summarized in Table 2, and the fits are shown as solid lines in Figure 6. For comparison, we also give $\tau_{\text{fly-by}}$, i.e., the time it would take undeflected reactants to move a distance comparable to the range over which the intermolecular interaction is significant (5 Å). Comparison of $\tau_{\text{collision}}$ and $\tau_{\text{fly-by}}$ provides a measure of how “sticky” the collisions are.

It should be noted that the osculating complex model assumes that the angular distribution depends *only* on rotation of the complex during $\tau_{\text{collision}}$. Of course, the angular distribution is also influenced by other factors such as the distribution of reactive collision geometries (impact parameters, reactant orientation) and how collision geometry maps to scattering angle. In the low- E_{col} , long- $\tau_{\text{collision}}$ limit, complex rotation is the dominant factor. In the high- E_{col} limit of impulsive collisions, collision geometry is the dominant factor. For this system at the highest E_{col} studied, $\tau_{\text{collision}} \approx 4 \cdot \tau_{\text{fly-by}}$, and both lifetime and geometry effects are likely to be significant.

IV. Discussion

The increase in σ_{CT} at low E_{col} is partly attributable to the increase in $\sigma_{\text{collision}}$, and this trivial contribution has been divided out in Figure 7, which shows the CT reaction efficiency ($\sigma_{\text{CT}}/\sigma_{\text{collision}}$) for ground-state NO_2^+ . The efficiency at our lowest E_{col} (0.07 eV) can be compared with the thermal rate constant¹³ of $2.9 \times 10^{-10} \text{ cm}^3 \text{ molecule}^{-1} \text{ s}^{-1}$, corresponding to $\sim 20\%$ reaction efficiency. Given that the width of our collision-energy spread is comparable to E_{col} at $E_{\text{col}} = 0.07 \text{ eV}$, we conclude that the beam and thermal results are consistent within the absolute uncertainties. A detailed comparison with drift tube results of Durup-Ferguson et al.¹⁴ is given in the final section. The efficiency has opposite E_{col} dependence at low and high E_{col} , with the transition occurring at $\sim 0.25 \text{ eV}$. This is just the energy where the v_{axial} distributions switch from symmetric to asymmetric, again suggesting that the mechanism at higher and lower E_{col} may be different. We therefore will address the CT mechanism for low and high E_{col} separately.

A. High-Energy Mechanism. As shown in Figure 4, the cross-section is nearly E_{col} -independent for all initial states at E_{col} above $\sim 0.25 \text{ eV}$. Over this energy range, the v_{axial} distributions become increasingly backward-peaked, indicating that CT occurs by a direct mechanism. In the limit of impulsive scattering at high E_{col} , the velocity distributions should depend mostly on the range of impact parameters (b) leading to CT. Because the charge is transferred in the collision, our definition of “backward” corresponds to small scattering angles, attributed to large b collisions, and “forward” corresponds to rebound scattering and small b collisions. The backward peak indicates that the largest component of the CT products is formed in collisions with b large enough that the scattering angle is less than 90° .

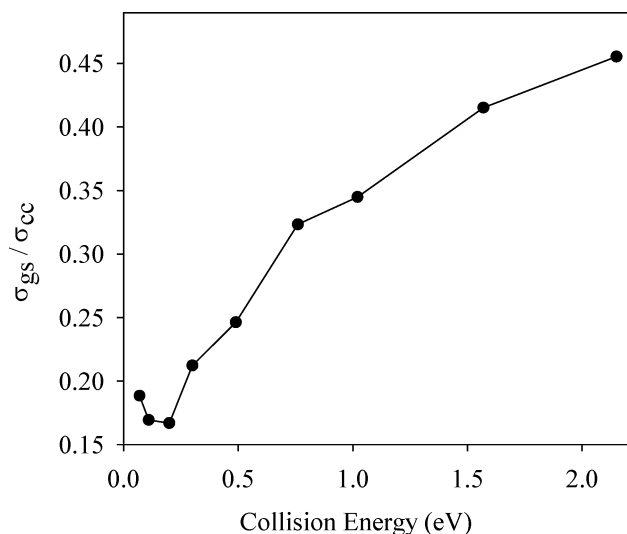
For the discussion below, we will somewhat artificially distinguish three ranges of collision impact parameters. “Small impact parameter” refers to nearly head-on collisions resulting in forward-scattered NO^+ . “Large impact parameter” refers to collisions with b large enough to generate backward-scattered NO^+ but small enough that there is a “real” collision, i.e. where the minimum reactant separation, R_{min} , becomes comparable to the hard-sphere radius, $R_{\text{HardSphere}}$. Finally, “long range” refers to collisions at such large impact parameters that $R_{\text{min}} > R_{\text{HardSphere}}$, but still in the range of significant inter-reactant potential energy.

Exoergic CT between polyatomic species is often possible even for such long-range collisions, and because forces are weak at long range, little momentum transfer can occur. The signature of such a long-range CT process is, therefore, product ions that are slow in the lab frame, i.e., strongly backscattered in the CM frame. If long-range CT is efficient, it will dominate the reaction, resulting in CT cross-sections substantially greater than $\sigma_{\text{HardSphere}}$ and v_{axial} distributions that are sharply backward-peaked.^{31–36} For the $\text{NO}_2^+ + \text{NO}$ system, the distributions

TABLE 2: NO⁺ Velocity Distribution Fit Results for the Osculating Complex Model

E_{col} (eV)	$\langle E_{\text{avail}} \rangle^a$ (eV)	$\langle E_{\text{recoil}} \rangle$ (eV)	$\langle E_{\text{recoil}} \rangle / \langle E_{\text{avail}} \rangle$ (%)	$\tau_{\text{collision}}$ (ps)	$\tau_{\text{fly-by}}^b$ (ps)	Vibs/ $\tau_{\text{fly-by}}^c$	$\langle E_{\text{recoil}} \rangle / \langle E_{\text{col}} \rangle$
0.09	0.45	0.09	20	>4.2	0.52	8.9	1.00
0.16	0.55	0.09	16	>3.6	0.35	6.7	0.39
0.26	0.62	0.11	18	2.3	0.30	5.2	0.38
0.48	0.86	0.16	19	1.0	0.22	3.8	0.32
0.71	1.09	0.32	29	0.67	0.18	3.2	0.43
0.96	1.34	0.45	33	0.59	0.15	2.7	0.46
1.55	1.88	0.77	41	0.48	0.12	2.1	0.50
2.04	2.42	1.07	44	0.40	0.11	1.9	0.52

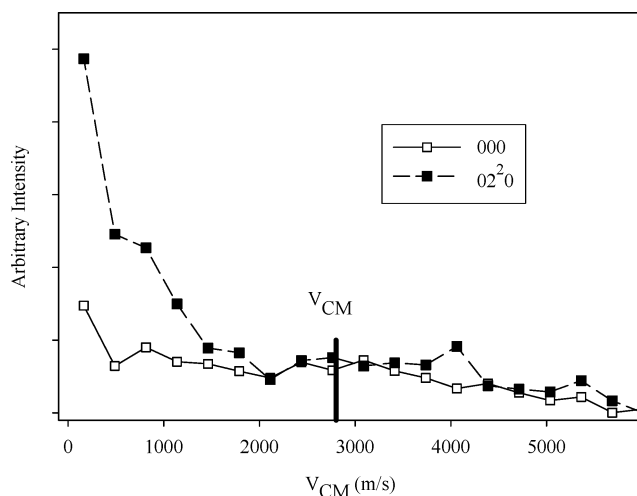
^a $\langle \rangle$ = mean value. ^b $\tau_{\text{fly-by}}$ defined as time for undeflected reactants to travel a relative distance of 5 Å. ^c Number of classical bend vibrational periods during $\tau_{\text{fly-by}}$.

**Figure 7.** Plot of the reaction efficiency vs collision energy for the ground state.

remain quite broad even at the highest energies, peaking far from $v_{\text{LAB}} = 0$, and with a large forward-scattered component. This observation indicates that long-range CT is not efficient in this system, consistent with our observation that the ground-state CT cross-section is less than half the collision cross-section. In fact, the small CT cross-section and large contribution of forward-scattered NO⁺ together indicate that ground-state CT is efficient only for small impact parameters. The reasons are discussed in the following section.

B. Vibrational Effects. The most obvious vibrational effect in this system is that the NO₂⁺ bending excitation strongly enhances CT, with an approximately linear dependence on the bending quantum number (Figure 5). Symmetric stretch (100) excitation has a similar effect to that of one quantum of the bend, despite having about twice the vibrational energy content. Finally, the highest-energy mode, the asymmetric stretch (001), has very little effect. The pattern of effects is nearly independent of E_{col} over the energy range studied, i.e., from $E_{\text{col}} < E_{\text{vib}}$ to $E_{\text{col}} \gg E_{\text{vib}}$.

The source of the bending enhancement can be seen in Figure 8, which compares the v_{axial} distributions at $E_{\text{col}} \approx 2$ eV for NO⁺ products from reaction of NO₂⁺ in its ground state and with (02²0) excitation. The v_{axial} distributions are normalized so that they correctly reproduce the relative CT cross-sections for the two states. Bending excitation has little effect on the forward-scattered portion of the distribution but substantially enhances backward-scattering. This result indicates that the CT probability for small impact parameter collisions is essentially unaffected by NO₂⁺ bending—not surprising because CT is quite efficient for such collisions. In contrast, for the larger impact

**Figure 8.** Normalized axial recoil velocity distributions for the CT from the ground state and bend overtone.

parameter collisions leading to backward scattering, CT is strongly enhanced. As a consequence, the CT cross-section increases to $\sim 80\%$ of $\sigma_{\text{HardSphere}}$ for the (02²0) state, compared to $\sim 45\%$ for the ground state. Note, however, that, even for the (02²0) state, both the magnitude of σ_{CT} and the broadness of the v_{axial} distribution show that CT is still quite inefficient for long-range collisions. The effect of the bending vibration is primarily to enhance CT in the large impact parameter range, i.e., in grazing/glancing collisions.

There are several ways to think about CT probability in medium- to long-range collisions. In the long-range limit, CT is simply an electronic transition, where the source and destination orbitals happen to be on different molecules. Therefore, the Franck–Condon factors coupling the initial state to energetically accessible product states are important. Furthermore, the intermolecular interaction at long range is too weak to allow much translational \leftrightarrow vibrational energy ($V \leftrightarrow T$) conversion, implying that the product vibrational state must be nearly resonant with the reactant state. In this system, the NO geometry is nearly unchanged during CT, but the NO₂ bend angle changes from 180° for NO₂⁺ to 134° in NO₂. Figure 9 shows the MP2/6-311G** bending potentials and bending energy levels for NO₂⁺ and NO₂, with the energy scale offset such that the difference between zero-point levels is equal to the CT exoergicity. It is clear that the NO₂⁺ ground state only has significant Franck–Condon overlap with energetically inaccessible NO₂ vibrational levels, thus explaining why long-range CT does not occur in this system. Even for the (020) levels studied, the overlaps with accessible states are negligible.

A model appropriate for CT at somewhat shorter ranges is based on crossing of the reactant and product potential energy

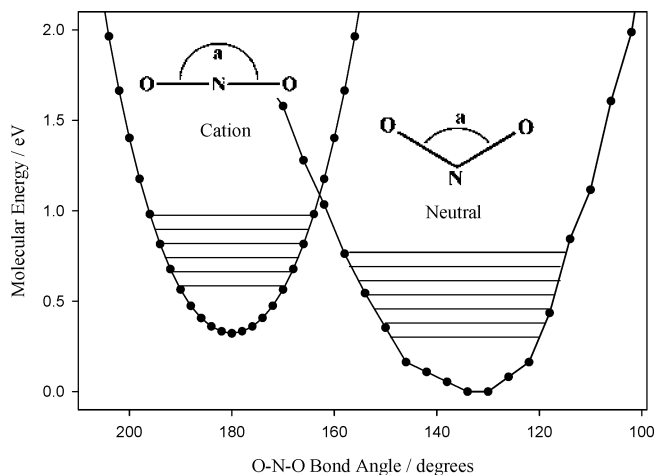


Figure 9. Bending potential for NO_2 and NO_2^+ calculated at the MP2/6-311G** level of theory. The curves are plotted so that the difference between zero-point levels equals the CT exoergicity.

surfaces. The curves in Figure 9 represent a cut along the NO_2 bending coordinate through the $\text{NO}_2^+ + \text{NO}$ and $\text{NO}_2 + \text{NO}^+$ potential surfaces at infinite reactant separation. As reactants approach, the crossing becomes avoided, resulting in a lower adiabatic surface consisting of $\text{NO}_2^+ + \text{NO}$ and $\text{NO}_2 + \text{NO}^+$ potential wells separated by a barrier. The height of this barrier decreases as the strength of the intermolecular interaction increases at decreasing reactant separations. For ground-state NO_2^+ , a low barrier is needed to allow significant “leakage” of the reactant wave function into the $\text{NO}_2 + \text{NO}^+$ potential well. A low barrier implies close reactant approach, which does not occur in large *b* collisions at high E_{col} . For NO_2^+ with bending excitation, significant CT can occur for a higher barrier, i.e., larger reactant separations, allowing CT to occur in larger impact parameter collisions. This effect enhances the CT cross-section and also leads to more backward-scattered product ions, as observed.

The asymmetric stretch (001) mode has essentially no effect, despite being the highest-frequency vibration. Both NO_2^+ and NO_2 have symmetric NO bond lengths, and the asymmetric stretch is not Franck–Condon-active, nor is there a surface crossing along this coordinate. Asymmetric stretching energy is, therefore, ineffective in driving the transition between the $\text{NO}_2^+ + \text{NO}$ and $\text{NO}_2 + \text{NO}^+$ regions of the potential surface.

It is interesting that the symmetric stretch (100) causes significant enhancement—comparable to that from (010) excitation. This enhancement may reflect the fact that there is a small change in bond length upon neutralization, $R(\text{NO}_2^+) = 1.143$ Å and $R(\text{NO}_2) = 1.203$ Å at the MP2/6-311g** level of theory, but it is probably more significant that the NO_2^+ and NO_2 bending normal modes include some change in bond length, and the NO_2 symmetric stretch normal mode involves some bending. Given that the symmetric stretch has more than twice the energy of the bend fundamental, some enhancement is not surprising. There is a complication, however. The NO_2^+ symmetric stretch is in Fermi resonance with the Σ symmetry (02^0_0) component of the bend overtone, as characterized by Matsui et al.³⁷

$$\Psi_{100} = 0.949\varphi_{100} - 0.316\varphi_{02^0_0}$$

$$\Psi_{02^0_0} = 0.316\varphi_{100} + 0.949\varphi_{02^0_0}$$

where the Ψ s represents the wave functions for the perturbed states, and the φ s are the zeroth-order symmetric stretch and

bend overtone functions. The squares of the coefficients show that each perturbed state has $\sim 10\%$ admixture of the other zeroth-order state, i.e., the “symmetric stretch” state populated in our experiment has $\sim 10\%$ bend overtone character. The large enhancement observed for bending excitation raises the question of whether the modest enhancement from “symmetric stretch” excitation might partly result from the bend overtone admixture. This issue can be assessed by comparison of the effects of the (02^0_0) and (02^2_0) excitations. If the symmetric stretch had no effect on CT, then the enhancement from the pure bend overtone, (02^2_0), should be larger than that from (02^0_0) excitation, where there is $\sim 10\%$ symmetric stretch character. Within experimental error, the two (02^0_0) and (02^2_0) states have identical effects (Figure 4), suggesting that the symmetric stretch does cause significant enhancement in its own right. This analysis is somewhat tentative because of the small symmetric stretch component in the (02^0_0) state; nonetheless, for the same reason, it is unlikely that the enhancement observed from exciting the symmetric stretch could result only from the 10% bend overtone admixture.

Figure 7 shows that in the high E_{col} regime ($E_{\text{col}} > \sim 0.25$ eV), where reaction is clearly direct, the ground-state CT efficiency is strongly dependent on E_{col} . The CT cross-section, itself, is essentially E_{col} -independent. Therefore, the efficiency behavior implies that the CT probability for small-to-medium impact parameters increases rapidly enough with increasing E_{col} to compensate for the decrease in the range of impact parameters leading to collisions. We propose the following elaboration of the CT mechanism discussed above: CT appears to be quite efficient for small impact parameter collisions, and there is no reason to expect strong collision energy effects for long-range collisions, which only sample the weak long-range potential. Therefore, the E_{col} effect must result from enhancement of CT in the large impact parameter range. Consider a long-range collision where CT does not occur during reactant approach. In the actual intimate collision, there is some probability for collisional excitation of NO and NO_2 vibrational modes, with the lowest-frequency mode (i.e., the NO_2^+ bend) most likely to be excited. During the subsequent separation of the collision partners, this bend excitation would enhance the charge-state mixing and therefore the net CT probability. Because the level of bend excitation presumably increases with E_{col} , the net effect is to increase CT efficiency at high E_{col} . For high levels of collisionally excited bending vibration, we expect that the wave function should freely explore both the $\text{NO}_2^+ - \text{NO}$ and $\text{NO}_2 - \text{NO}^+$ regions of the lowest adiabatic surface. In this case, the net CT probability is simply the probability that the system ends up trapped in the lower-energy $\text{NO}_2 - \text{NO}^+$ well as the collision partners separate. Given the energetics of the two charge states, we might expect a limiting high- E_{col} CT efficiency somewhat above 50%—consistent with the apparent trend in measured efficiency.

It is interesting to note that Clemmer and Armentrout observed that for the reverse reaction, i.e., endoergic CT of NO^+ with NO_2 , the cross-section is enhanced by E_{col} . Of course for an endoergic reaction, it is not surprising that additional energy in any form increases reaction efficiency, and the question is how collision energy is converted to whatever form is required to drive the electronic transition. NO_2 bending excitation should enhance $\text{NO}^+ + \text{NO}_2$ CT for the same reasons that NO_2^+ bending enhances CT in $\text{NO}_2^+ + \text{NO}$. The discussion above suggests that a likely mechanism might be collisional excitation of the NO_2 bend, leading to enhanced CT probability as the collision partners separate.

C. Reaction at Low Energies. The forward–backward symmetric v_{axial} distributions observed for $E_{\text{col}} \leq \sim 0.25$ eV raise the possibility that growth of a complex-mediated mechanism might account for the observation that CT efficiency increases sharply at low E_{col} . From the fitting results in Table 2, it can be seen that $\tau_{\text{collision}}$ on the order of a few picoseconds would be required in order to yield symmetric distributions by complex rotation. The most strongly bound complex found in our quantum chemistry calculations is the productlike complex shown in Figure 3, which is bound by only 0.34 eV with respect to products at the QCISD(T) level and by 0.43 eV at the G3 level of theory. To see if this complex might be stable enough to account for $\tau_{\text{collision}}$, we estimated the lifetime using RRKM theory.³⁸ Ab initio vibrational frequencies and moments of inertia were used for the complex, and orbiting transition states (TSs) were assumed for dissociation to reactants and products.³⁹ As noted, the complex is productlike, i.e., the charge is mostly on the NO moiety. There is no reason, therefore, to assume any sort of barrier along the coordinate for dissociation to products. For the purpose of estimating the rate of dissociation back to reactants, we also assumed that there is no bottleneck related to the required electronic transition. This assumption is actually not important, because the lifetime is mostly determined by dissociation to the more energetically favorable product channel. The lifetimes from the productlike complex are less than 100 fs, even at our lowest E_{col} —far too short to account for $\tau_{\text{collision}}$. Furthermore, even if this complex had substantial lifetime, it could not account for the increased reaction efficiency at low E_{col} . To influence reactivity, a complex must enhance passage through the rate-limiting step along the reaction coordinate, which in this system appears to be the actual CT event. This productlike complex statistically dissociates almost entirely to CT products; therefore, it should have no effect on CT efficiency.

If there were a reactantlike complex with a significant lifetime, this could account for both the forward–backward symmetry and the increased CT efficiency. A reactantlike $\text{NO}_2^+ - \text{NO}$ complex corresponds to an electronically excited state of the $[\text{NO}_2 - \text{NO}]^+$ system, but given the large change in ONO angle accompanying the $\text{NO}_2^+ - \text{NO} \rightarrow \text{NO}_2 - \text{NO}^+$ transition (Figure 9), it is conceivable that such a complex could have a significant lifetime. The reactantlike complex shown in Figure 3 was found as follows: Several different $[\text{ONO} - \text{NO}]^+$ starting geometries were optimized at the MP2/6-31G* level under the constraint of a nearly linear (179°) ONO moiety, all converging to a structure similar to that in Figure 3. We then attempted to optimize the resulting structure with the ONO angle unfrozen, with the result that the ONO moiety remains nearly linear (ONO angle 177°). Unfortunately, neither the Berny nor DIIS optimization algorithms were able to converge to an optimized structure in several hundred cycles. During optimization, the energy initially decreased smoothly toward an asymptotic value, as expected, but both algorithms got stuck “hunting” around a small range of geometries, with 1–2% variations in various bond lengths and angles and corresponding energy variations on the order of 50 ppm. The problem does not appear to be instability in the electronic configuration. Both the charge distribution and character of the singly occupied molecular orbital were essentially unchanged during the “hunting” process. The coefficient of the Hartree–Fock configuration was ~ 0.94 in a CASSCF(9,12) calculation at the minimum-energy geometry, suggesting that the MP2 method should be adequate. The convergence problem is apparently related to the shape of the potential near the shallow minimum.

The energy reported in Figure 3 is from a QCISD(T)/6-311+G** single-point calculation at the MP2 geometry with the lowest energy. The vibrational frequency distribution associated with this “nearly optimized” structure looks quite reasonable, with one exception. There are four modes associated with the NO_2^+ moiety, four modes corresponding to inter-reactant vibrations, and one for the NO stretch. The low-frequency modes are in the $70\text{--}250\text{ cm}^{-1}$ range expected from comparison with the converged productlike complex, the NO_2^+ frequencies close to those in free NO_2^+ , and the obvious problem is that the stretch frequency for the NO moiety is $\sim 25\%$ too high. For ZPE correction of the energy and for frequencies in the RRKM calculation, we used these calculated frequencies but replaced the spurious NO stretch frequency with the value for free NO.

The properties of this calculated complex should be thought of as qualitative, but it is still useful to estimate the RRKM lifetime. In this case, we simply calculated the lifetime with respect to dissociation back to reactants, because we have no way to estimate the time scale for transition to products. The lifetimes turn out to be well below 100 fs for all values of reactant orbital angular momenta, even for our lowest E_{col} . Again, it appears that the potential surface does not support a mechanistically significant complex, and we conclude that CT is direct at all energies.

It is possible to rationalize the symmetric v_{axial} distributions and increased CT efficiency at low E_{col} within a direct CT mechanism. Even if a statistical complex does not form, it is clear that the collision time (see $\tau_{\text{fly-by}}$, Table 2) must increase as E_{col} is decreased, and it may be that CT is enhanced at low E_{col} simply because reactants spend more time in close proximity, allowing more time for the wave function to “leak” into the product well. The symmetric v_{axial} distributions may simply indicate that the kinetic energy release in the CT reaction at low E_{col} is simply too small for us to resolve any asymmetry in the angular distribution.

D. Comparison with Drift Tube Results. As noted in the Introduction, Durup-Ferguson et al.¹⁴ reported a drift tube study of the $\text{NO}_2^+ + \text{NO}$ CT reaction where He and Ar buffer gases were used in conjunction with a variable drift potential to probe the effects of collision energy and vibrational excitation. The idea in these experiments is that, as the drift potential is increased, the average drift velocity of the ions increases, thus increasing the average collision energy. In addition, the ion–buffer gas collisions can lead to rotational and vibrational excitation of the ions. For NO_2^+ drifting at a particular velocity, the collisions with helium buffer gas atoms have much lower reduced mass, and hence collision energy, than those with the NO reactant. As a consequence, the NO_2^+ internal energy distribution (set by $\text{NO}_2^+ - \text{He}$ collisions) is relatively cold in comparison to the $\text{NO}_2^+ - \text{NO}$ collision energy. For the heavier Ar buffer, the degree of NO_2^+ internal excitation is much higher for the same $\text{NO}_2^+ - \text{NO}$ collision energy. Thus, by comparing reaction rates in the He and Ar buffer, $k(\text{He})$ and $k(\text{Ar})$, at the same E_{col} , it is possible to infer the effects of internal excitation. Our analysis of the drift tube data follows the discussion in the recent review paper of Viggiano and Morris.⁴⁰

The Durup-Ferguson results for $k(\text{He})$ and $k(\text{Ar})$ are shown as the solid black symbols in the top frame of Figure 10. Note that, at low E_{col} , where both the He and Ar experiments are essentially thermal, they are identical within the 30% uncertainty stated in the paper. As E_{col} is increased, $k(\text{He})$ drops through a minimum, then increases. The $k(\text{Ar})$ data rapidly diverge from $k(\text{He})$, as a consequence of the higher internal energy distribution

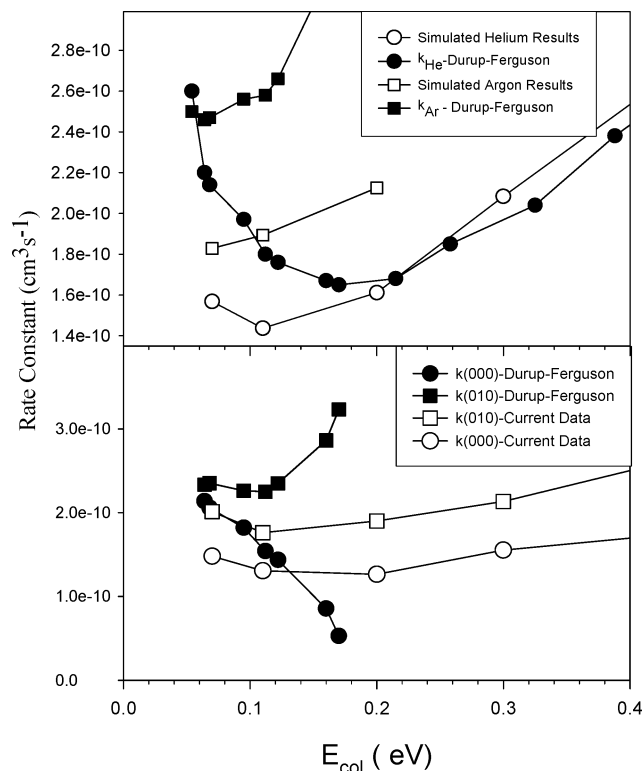


Figure 10. Comparison of drift tube rate constants with our results. Top frame: Solid symbols are raw drift tube data for $k(\text{He})$ and $k(\text{Ar})$. Open symbols are simulations of the drift tube results based on our absolute cross-sections. Lower frame: Open symbols are our state-specific cross-sections converted to specific rate constants. Filled symbols are state-specific rate constants extracted by comparing $k(\text{He})$ and $k(\text{Ar})$ from the drift tube experiments.

excited in the argon case. The effect was attributed to excitation of the lowest-energy vibrational mode, i.e., the NO_2^+ bend.

We have two ways to compare our results with the drift tube data. In the top frame of the figure, we used our measured state-specific cross-sections to simulate the drift tube rate constants, assuming that rotational effects are negligible. The simulation was done by taking the E_{col} values in the drift tube study and calculating the associated vibrational temperatures expected for both He and Ar buffer gas, using the procedures given by Viggiano and Morris.⁴⁰ For each E_{col} point, the vibrational temperature was used to calculate the vibrational populations, and then, the rate constant was calculated as the population-weighted average of the rate constants for each vibrational state at E_{col} . These state-specific rate constants were obtained by simply multiplying our cross-sections at each E_{col} by the associated relative velocities. For $k(\text{He})$, where there is little vibrational excitation in the drift tube, the agreement is excellent for $E_{\text{col}} > 0.1$ eV. The discrepancy at lower E_{col} probably reflects the fact that the E_{col} distributions are different in the beam and drift tube experiments, and the cross-section is strongly E_{col} -dependent at low E_{col} (Figure 4). For $k(\text{Ar})$, we have only attempted to simulate the results for low E_{col} , because we have not measured cross-sections for the high vibrational levels populated in Ar at high E_{col} . Even for low E_{col} , there is a $\sim 40\%$ discrepancy between the $k(\text{Ar})$ values based on our cross-sections and the drift tube $k(\text{Ar})$ results.

The other approach to comparing the two experiments is to use the data in each to calculate state-specific rate constants. For our cross-section data, we simply multiply the state-specific cross-sections by the relative velocity at each E_{col} , and the lower frame of the figure shows the resulting rate constants for NO_2^+

in its ground state, $k(000)$, and with one quantum of bend excitation, $k(010)$, as open symbols. Extracting state-specific rates from the drift tube data is more difficult. For a particular E_{col} and buffer gas, we can write (using He for example)

$$k(\text{He}, E_{\text{col}}) = f_{000} \cdot k(000, E_{\text{col}}) + f_{010} \cdot k(010, E_{\text{col}}) + f_{020} \cdot k(020, E_{\text{col}}) + f_{100} \cdot k(100, E_{\text{col}}) + \dots$$

where f_{nml} and $k(nml, E_{\text{col}})$ are the population and rate constant for state (nml) at E_{col} . Because He and Ar give different vibrational temperatures at each E_{col} , there is sufficient information to extract $k(000)$ and $k(010)$, if we can assume that only these two lowest-energy states are significantly populated. Unfortunately, except for the lowest drift tube E_{col} values, this assumption is not good. To get around this problem, we use our state-specific cross-sections to rewrite the rate constants for the higher-energy vibrational states in terms of $k(010)$. For example, our results show that $\sigma(020) = 1.97 \cdot \sigma(010)$, therefore $k(020) = 1.97 \cdot k(010)$. By making such substitutions for all states except (000) and (010) , we can solve the expressions for $k(\text{He}, E_{\text{col}})$ and $k(\text{Ar}, E_{\text{col}})$ to extract $k(000, E_{\text{col}})$ and $k(010, E_{\text{col}})$. This analysis has been done for E_{col} values up to the point where there starts to be significant population of (nml) states for which we have no cross-sections. The results are plotted in the lower frame with filled symbols.

The drift tube results correctly predict that $k(010)$ is larger than $k(000)$; however, the magnitude of the enhancement and its E_{col} dependence are in poor agreement with our direct measurements. There are several factors that might account for the discrepancy. The E_{col} distributions are different for the beam and drift tube experiments, and there are also differences for He and Ar buffer gas. This issue is probably not important, because our $k(000)$ and $k(010)$ results (open symbols, lower frame) show that reactivity is weakly E_{col} -dependent in this E_{col} range. We have also ignored rotational effects in the analysis of the drift tube results, and if rotation strongly enhanced CT, that would diminish the difference between the extracted $k(000)$ and $k(010)$ curves. Rotational effects on ion-molecule reactions have not been studied extensively. In beams, it is typically only possible to access low J states, and the effects have been negligible except at very low E_{col} or very near the threshold for endoergic reactions (see Liu et al.⁴¹ and references therein). The most useful information for the higher rotational temperatures of interest here comes from variable temperature drift tube work, and this area has been reviewed recently by Viggiano and Morris.⁴⁰ They report rotational effects to be small, i.e., less than the 15% experimental uncertainty, except in a few reactions such as $\text{Kr}^+ + \text{HCl}$ or HD, and $\text{OH}^- + \text{D}_2$, where one or both reactants have large rotational constants. There is no reason to expect that exoergic CT should depend significantly on rotational state in the E_{col} regime of interest; thus, we tend to discount this explanation.

We feel the most likely explanation is that the actual vibrational populations in the drift tube are not well-represented by the calculated vibrational temperature. It appears that for $E_{\text{col}} > 0.1$ eV, the drift tube analysis underestimates the difference in vibrational excitation between helium and argon and, as a consequence, overestimates the difference between $k(000)$ and $k(010)$. Because the helium vibrational temperatures are relatively low at all E_{col} , the problem most likely reflects errors in assuming a thermal vibrational distribution for the argon buffer gas, particularly at higher drift velocities. This behavior is not surprising: For argon, the ion-buffer collisions are less frequent but considerably more energetic than with

helium, and it would not be surprising to see some excitation of high vibrational levels, particularly bending overtones, which our results indicate to be highly reactive.

V. Conclusions

Two-color, three-photon ionization of NO₂ is suitable for producing intense pulsed beams of vibrationally state-selected NO₂⁺ that we plan to exploit in a number of reaction studies. Charge transfer of NO₂⁺ with NO is strongly enhanced by excitation of its bending vibration, more weakly enhanced by symmetric stretch excitation, and unaffected by excitation of the asymmetric stretch. A Franck–Condon picture is not useful in this system, because the NO₂ geometry change is too large. Instead, we propose a curve crossing mechanism, with the CT transition driven by motion along the NO₂ bend coordinate.

Acknowledgment. The authors gratefully acknowledge Edward Grant and Stephen T. Pratt for helpful suggestions and discussion regarding NO₂ spectroscopy, and for providing prepublication access to their photoelectron spectroscopy results. We are also grateful to Albert Viggiano for suggesting the comparison with the Durup-Ferguson drift tube results, and for his help in calculating the drift tube vibrational temperatures. This work is supported by the National Science Foundation under grant CHE-0110318.

References and Notes

- (1) Bell, P.; Aguirre, F.; Grant, E. R.; Pratt, S. T. *J. Phys. Chem. A* **2004**, *108*, 9645.
- (2) Ausloos, P.; Lias, S. G. *Int. J. Chem. Kinet.* **1978**, *10*, 657.
- (3) Cacace, F.; De Petris, G.; Pepi, F.; Angelelli, F. *Proc. Natl. Acad. Sci. U.S.A.* **1995**, *92*, 8635.
- (4) Cacace, F.; de Petris, G.; Pepi, F.; Rossi, I.; Venturini, A. *J. Amer. Chem. Soc.* **1996**, *118*, 12719.
- (5) Chen, L.; Xiao, H.; Xiao, J.; Gong, X. *J. Phys. Chem. A* **2003**, *107*, 11440.
- (6) Hasegawa, K.; Kaneko, H.; Ogawa, T. *Bull. Chem. Soc. Jpn.* **2004**, *77*, 147.
- (7) Moodie, R. B.; Schofield, K.; Taylor, P. G. *J. Chem. Soc., Perkin Trans. 2* **1979**, 133.
- (8) Morrison, J. D.; Stanney, K.; Tedder, J. M. *J. Chem. Soc., Perkin Trans. 2* **1981**, 967.
- (9) Peluso, A.; Del Re, G. *J. Phys. Chem.* **1996**, *100*, 5303.
- (10) Rosokha, S. V.; Kochi, J. K. *J. Org. Chem.* **2002**, *67*, 1727.
- (11) Ross, D. S.; Kuhlmann, K. F.; Malhotra, R. *J. Am. Chem. Soc.* **1983**, *105*, 4299.
- (12) Clemmer, D. E.; Armentrout, P. B. *J. Chem. Phys.* **1992**, *97*, 2451.
- (13) Fehsenfeld, F. C.; Ferguson, E. E.; Mosesman, M. A. *Chem. Phys. Lett.* **1969**, *4*, 73.
- (14) Durup-Ferguson, M.; Boehring, H.; Fahey, D. W.; Ferguson, E. E. *J. Chem. Phys.* **1983**, *79*, 265.
- (15) Bryant, G. P.; Jiang, Y.; Martin, M.; Grant, E. R. *J. Chem. Phys.* **1994**, *101*, 7199.
- (16) Matsui, H.; Mayer, E. E.; Grant, E. R. *J. Mol. Spectrosc.* **1996**, *175*, 203.
- (17) Kim, H.-T.; Anderson, S. L. *J. Chem. Phys.* **2001**, *114*, 3018.
- (18) Liu, J.; Kim, H.-T.; Anderson, S. L. *J. Chem. Phys.* **2001**, *114*, 9797.
- (19) Chiu, Y.-H.; Fu, H.; Huang, J.-T.; Anderson, S. L. *J. Chem. Phys.* **1995**, *102*, 1199.
- (20) Liu, J.; Van Devener, B.; Anderson, S. L. *J. Chem. Phys.* **2002**, *116*, 5530.
- (21) Herzberg, G. *Molecular Spectra and Molecular Structure III. Electronic Spectra and Electronic Structure of Polyatomic Molecules*; Van Nostrand Reinhold: New York, 1966.
- (22) Ervin, K. M.; Armentrout, P. B. *J. Chem. Phys.* **1985**, *83*, 166.
- (23) Chupka, W. A.; Russell, M. E.; Refaey, K. *J. Chem. Phys.* **1968**, *48*, 1518.
- (24) Liao, C. L.; Liao, C. X.; Ng, C. Y. *J. Chem. Phys.* **1984**, *81*, 5672.
- (25) Gerlich, D.; Rox, T. Z. *Phys. D: At., Mol. Clusters* **1989**, *13*, 259.
- (26) Glenwinkel-Meyer, T.; Gerlich, D. *Isr. J. Chem.* **1997**, *37*, 343.
- (27) Softley, T. P.; Mackenzie, S. R.; Merkt, F.; Rolland, D. *Adv. Chem. Phys.* **1997**, *101*, 667.
- (28) Green, R. J.; Kim, H.-T.; Qian, J.; Anderson, S. L. *J. Chem. Phys.* **2000**, *113*, 3002.
- (29) Lias, S. G.; Bartmess, J. E.; Liebman, J. F.; Holmes, J. L.; Levin, R. D.; Mallard, W. G. Ion Energetics Data. In *NIST Chemistry WebBook*; NIST Standard Reference Database Number 69; Mallard, W. G., Linstrom, P. J., Eds.; National Institute of Standards and Technology: Gaithersburg, MD, 2000; <http://webbook.nist.gov>.
- (30) Fisk, G. A.; McDonald, J. D.; Herschbach, D. R. *Discuss. Faraday Soc.* **1967**, *44*, 228.
- (31) Anderson, S. L.; Turner, T.; Mahan, B. H.; Lee, Y. T. *J. Chem. Phys.* **1982**, *77*, 1842.
- (32) Chiu, Y.-H.; Fu, H.; Huang, J.-T.; Anderson, S. L. *J. Chem. Phys.* **1996**, *105*, 3089.
- (33) Qian, J.; Fu, H.; Anderson, S. L. *J. Phys. Chem.* **1997**, *101*, 6504.
- (34) Liu, J.; Devener, B. V.; Anderson, S. L. *J. Chem. Phys.* **2002**, *117*, 8292.
- (35) Liu, J.; Uselman, B.; Van Devener, B.; Anderson, S. L. *J. Phys. Chem. A* **2004**, *108*, 9945.
- (36) Liu, J.; Van Devener, B.; Anderson, S. L. *J. Chem. Phys.* **2004**, *121*, 11746.
- (37) Matsui, H.; Behm, J. M.; Grant, E. R. *Int. J. Mass Spectrom. Ion Processes* **1996**, *159*, 37.
- (38) Zhu, L.; Hase, W. L. A general RRKM program (QCPE 644). In *Quantum Chemistry Program Exchange*; Chemistry Department, University of Indiana: Bloomington, IN, 1993.
- (39) Rodgers, M. T.; Ervin, K. M.; Armentrout, P. B. *J. Chem. Phys.* **1997**, *106*, 4499.
- (40) Viggiano, A. A.; Morris, R. A. *J. Phys. Chem.* **1996**, *100*, 19227.
- (41) Liu, J.; Devener, B. V.; Anderson, S. L. *J. Chem. Phys.* **2003**, *119*, 200.